Journal of Petroleum Science and Engineering 215 (2022) 110730

Contents lists available at ScienceDirect

Journal of Petroleum Science and Engineering

journal homepage: www.elsevier.com/locate/petrol

Geochemistry and depositional environment of the Mesoproterozoic Xiamaling shales, northern North China

Jin Wu [a,b], Hao Li [c], Fariborz Goodarzi [d], Xu Min [a,b], Weixun Cao [a,b], Lijuan Huang [a,e], Yueyang Pan [a,b], Qingyong Luo [a,b,*]

[a] State Key Laboratory of Petroleum Resources and Prospecting, China University of Petroleum (Beijing), Beijing, 102249, China
[b] College of Geoscience, China University of Petroleum (Beijing), Beijing, 102249, China
[c] Wuxi Institute of Petroleum Geology of SINOPEC, Wuxi, 214126, China
[d] Environmental and Energy Research Group, FG & Partners Ltd., 219 Hawkside Mews NW, Calgary, AB T3G 3J4, Canada
[e] Suichang Mineral and Geological Monitoring Center, Suichang, Lishui, 323300, China

ARTICLE INFO

Keywords:
Geochemistry
Depositional environment
Xiamaling shales
Mesoproterozoic

ABSTRACT

The Mesoproterozoic Xiamaling shales from Xiahuayuan area, southeastern Xuanlong sag, Northern China, were examined the elemental analysis by applying the inductively coupled plasma-mass spectrometry (ICP–MS). The Xiamaling shales have good to excellent oil hydrocarbon generation potential with type II kerogenas demonstrated by high content of alginate macerals, TOC, HI, $S_1 + S_2$ and extractable organic matter (EOM). The Xiamaling shales were deposited under a marine environment according to boron (B) (56–111 ppm) and other trace elements concentration, which is consistent with the geological settings. These shales can be classified into three types: (1) Type I is a coastal facies, which is influenced by fresh riverine water and has low B content of 56–61 ppm; (2) Type II is a marginal marine with B content of 73–79 ppm; and (3) type III has high B content of 111 ppm, typical of a brackish, and open marine environment.

The Xiamaling shales have high B (>50 ppm), low Na, Ca, Ce, Mn, and rare earth elements (REEs). According to the elemental composition and ratios, the Xiamaling sediments were derived from the felsic source, which has suffered from moderate to strong chemical weathering based on the CIA, ICV, and PIA values. The Xiamaling marine shales were mostly deposited under dysoxic-anoxic conditions. The paleoclimate during the deposition of the Xiamaling shales was warm and humid based on the cross plots of Sr/Ca vs Mn/Ca values and Sr/Cu vs Rb/Sr ratios. Their total REE (ΣREE) contents increase from coastal towards the open marine zone. The Xiamaling shales display a negative Ce anomaly, representative of marine shale, and show a negative Eu anomaly, which is representative of lacustrine oil shale and the Post-Archean Australian Shale (PAAS) and is different from typical marine shale of younger age, indicating the influx of terrestrial sediment.

CRediT (Contributor roles taxonomy) author statement

Jin Wu: Conceptualization, Methodology, Data curation, Writing - original draft. Visualization, Investigation, Writing - review & editing, Funding acquisition. Hao Li: Supervision, Data curation, Writing - review & editing. Fariborz Goodarzi: Supervision, Review & Editing, Xu Min: Sample collection, Data curation, Writing - review & editing, Weixun Cao: Sample collection, Data curation, Lijuan Huang: Sample collection, Data curation, Yueyang Pan: Sample collection, Qingyong Luo: Conceptualization, Resources, Supervision, Project administration, Funding acquisition.

1. Introduction

The Mesoproterozoic Xiamaling shales are well known as the oldest, low thermal maturity source rocks, with well–preserved organic matter (OM) (Luo et al., 2015a; Wang et al., 2018; Zhang et al., 2017, 2018). It provides an opportunity to study the paleoenvironment, paleoclimate, paleoproductivity, characteristics, compositions, and genesis of OM. The Mesoproterozoic OM-rich sediments are important hydrocarbon source rocks worldwide (Crick et al., 1988, 1992; Luo et al., 2013, 2016; Wang et al., 2018; Zhang et al., 2017, 2019). Previous studies on the Mesoproterozoic organic-rich sediments mainly focus on paleoenvironment,

* Corresponding author. State Key Laboratory of Petroleum Resources and Prospecting, China University of Petroleum, Changping, Beijing, 102249, China.
E-mail address: qingyong.luo@cup.edu.cn (Q. Luo).

https://doi.org/10.1016/j.petrol.2022.110730
Received 16 April 2021; Received in revised form 28 April 2022; Accepted 1 June 2022
Available online 6 June 2022

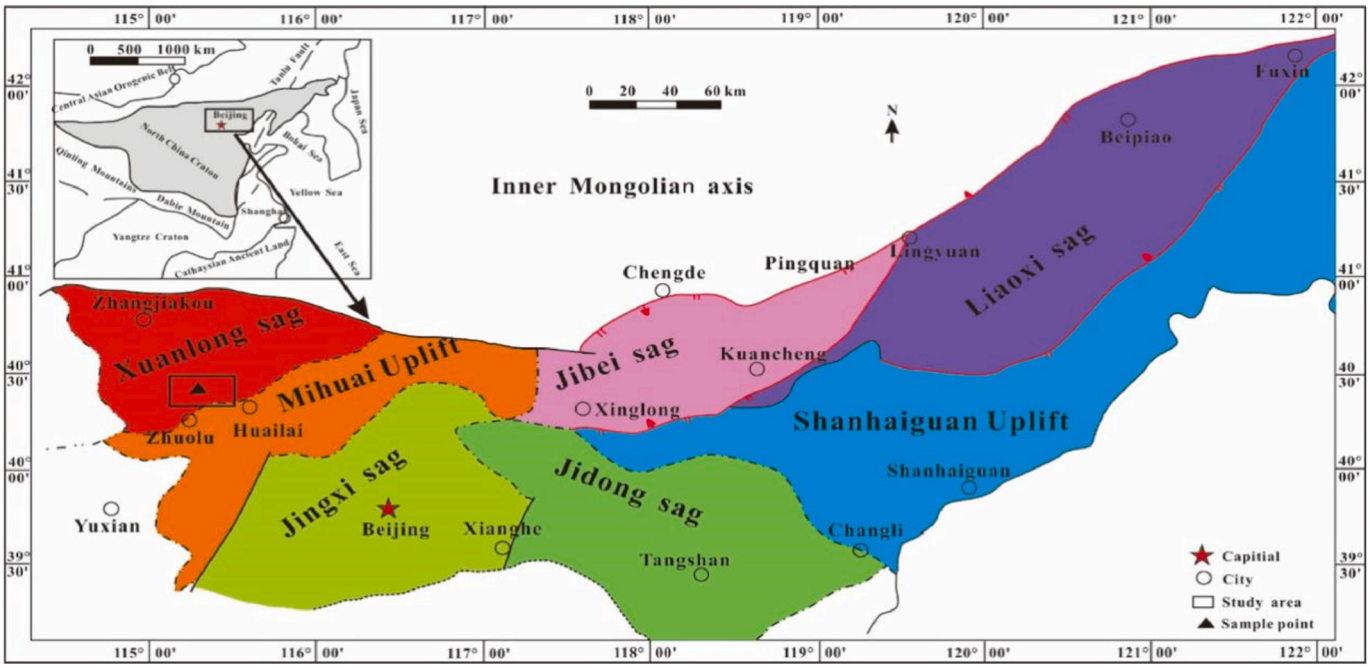

Fig. 1. Tectonic units in the Yanshan area and the sampling locations (after Luo et al., 2014).

paleoclimate, and organic geochemistry (Blumenberg et al., 2012; Delpomdor et al., 2013a, 2013b; Diamond et al., 2018; Frank et al., 1997; Luo et al., 2016; Ma et al., 2017; Mitchell and Sheldon, 2010; Rashid et al., 2018; Wang et al., 2017, 2018; Zhang et al., 2015, 2016a, 2016b, 2017, 2019). The Mesoproterozoic paleoenvironment and paleoclimate inferred from the Xiamaling shales have caught extensive attention in recent decades (Diamond et al., 2018; Wang et al., 2017, 2018; Zhang et al., 2015, 2016a, 2016b, 2017, 2019). The oxygen concentration in the atmosphere during the deposition of the Xiamaling shales has reached up to 4% of the present-day level, which was sufficient for the animal respiration and the existence of green bacteria in sedimentary water column (Zhang et al., 2016a). Canfield et al. (2018) reported iron formation in the Xiamaling Formation, similar to the banded iron formation (BIF) in the late–Archean sediments, which is benefited from the low H_2S and high Fe^{2+} concentrations. However, it is still controversial whether the depositional environment of the Xiamaling shale belongs to an open or a restricted closed marine basin (Diamond et al., 2018; Zhang et al., 2019).

Geochemistry of marine shale is different from the terrestrial, such as the lacustrine, due to different organic input in addition to difference in sedimentation and weathering processes, which is more evident in lacustrine than marine. A lacustrine source rock is influenced by water input and discharge variation, tectonic activity, and climatic variation (Goodarzi et al., 2019a, 2019b, 2020, 2021).

There is very little data on marine shale geochemistry, particularly of the Mesoproterozoic age (1400 Ma). The present paper documents the elemental composition of marine Xiamaling shales and their comparison with the Canadian lacustrine Big Marsh and marine Second White Speckled oil shale (Bloch et al., 1999; Goodarzi et al., 2019a, 2020; Leleyter and Probst, 1999; Macrae et al., 1992).

2. Geological setting

The Yanshan area, known as “Yanshan Subsidence Zone” contains “two uplifts and five sags” tectonic units, i.e., Xuanlong sag, Mihuai uplift, Jingxi sag, Jidong sag, Jibei sag, Shanhaiguan uplift, and Liaoxi sag from west to east (Luo et al., 2014) (Fig. 1). The development of the Yanshan aulacogen has a significant influence on the geotectonic evolvement of North China in Meso–Neoproterozoic (Luo et al., 2015b; Wang and Qiao, 1984). The studied area is located in the Xiahuayuan area, southeastern Xuanlong sag (Fig. 1).

The North China region is one of the most developed and best-preserved areas of the Meso–Neoproterozoic sediments in China. The Meso–Neoproterozoic is subdivided into three groups, i.e., the Changcheng Group, Jixian Group, and Qingbaikou Group (Fig. 2). The Jixian Group consists of the Wumishan, Hongshuizhuang, Tieling, and Xiamaling Formation. There is an angular unconformably contact between Xiamaling Formation and overlying Changlongshan Formation. The age of the Xiamaling Formation ranges from ~1.40 to ~1.35 Ga on the basis of baddeleyite and zircon dating (Zhang et al., 2009, 2015). The Xiamaling Formation was deposited under a quiet, sedimentary water environment and included a series of black marine OM–rich shales (Zhang et al., 2015). During the Xiamaling Formation sedimentary period, the North China plates, paleolatitude ranges from 10°N to 30°N (Zhang et al., 2012b, 2017). The alternating lithology of the Xiamaling Formation mainly consists of black shale, sandy shale, siltstone, siliceous rock, and clay rock. Furthermore, a series of gabbro–diabase rocks have intruded into the Xiamaling Formation, which is due to the North China plate separation from the Columbia supercontinent (Meng et al., 2011; Zhang et al., 2012a). The sediments in Xiamaling Formation have experienced low burial temperatures (≤90 °C) with immature to early thermal mature in Zhangjiakou area (Zhang et al., 2015).

3. Samples and methods

Seven shale samples were retrieved from the Xiamaling Formation exposed at the Xiahuayuan, northern North China (Fig. 1). The weathered surfaces of the samples were cut to ensure that the samples are fresh and free of contamination, then the samples were ground to 100 mesh.

The inorganic carbon of 100 mg power sediments was cleared with dilute HCl, and the residue was washed repetitiously with deionized water and dried. The TOC of the shales was examined by Leco CS–230 analyzer.

The elemental concentration of the shales was determined using ICP–MS with an accuracy of ± 5–10% (relative), and inductively coupled plasma–optical emission spectrometry (ICP–OES) with an accuracy of ± 5–10% (relative) in the Guiyang Institute of Geochemistry, Chinese Academy of Sciences as reported by Qi et al. (2000). The

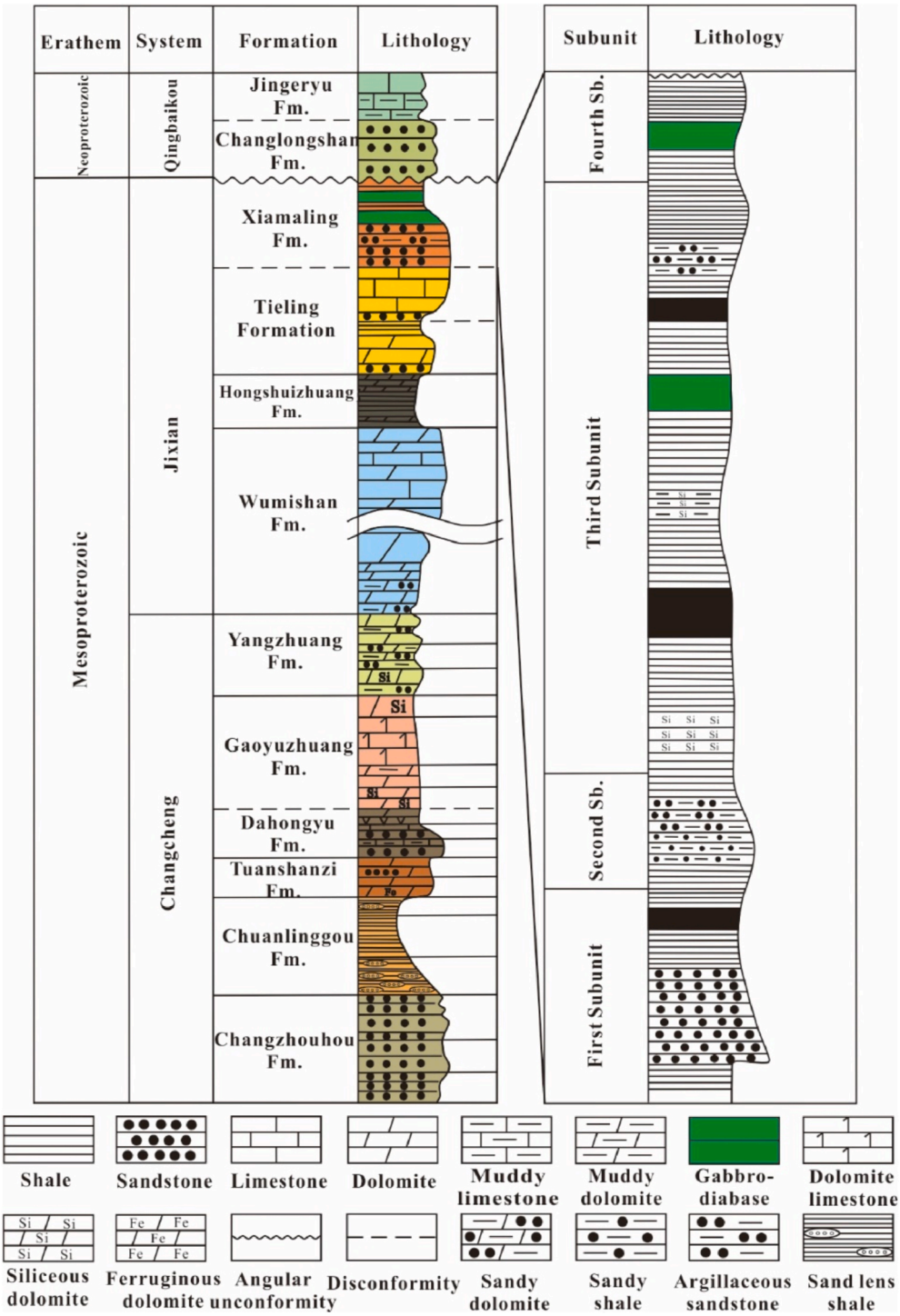

Fig. 2. Stratigraphic column of the Meso–Neoproterozoic and the Xiamaling Formation in the Yanshan region (after Luo et al., 2013).

distribution modes of REE were acquired by determining their content normalized to the PAAS (Taylor and McLennan, 1985). The enrichment degree of U and Mo was characterized by the enrichment factors (EF), where $X_{EF} = [(X/Al)_{sample}/(X/Al)_{PAAS}]$, Al and X are the percentage content of elements Al and X, respectively (Algeo and Tribovillard, 2009). The chondrite–normalized (CN) Eu anomaly (Eu_{an}) was obtained by the following formula: $Eu_{an} = Eu/(Sm \times Gd)^{1/2}$ (Cullers and Graf, 1984; Taylor and McLennan, 1985). The chemical index of alteration (CIA) and plagioclase index of alternation (PIA) are calculated by the following formulas: $CIA = \{Al_2O_3/(Al_2O_3 + CaO^* + Na_2O + K_2O)\} \times 100$, $PIA = \{(Al_2O_3–K_2O)/((Al_2O_3–K_2O) + CaO^* + Na_2O)\} \times 100$ (Fedo et al., 1995; Nesbitt and Young, 1982). The units of the oxides in the formulas of CIA and PIA are all mole. CaO* refers to the content of Ca in silicate, but excluding the non–silicate such as carbonates and phosphates (McLennan et al., 1993). The index of compositional variation (ICV) is obtained from the following equation: $ICV= (CaO + Na_2O + K_2O + Fe_2O_3 + MgO + MnO + TiO_2)/Al_2O_3$ (Varma et al., 2018).

Table 1
TOC and rock pyrolysis data of the Xiamaling shales.

Sample	Lithology	TOC wt %	S_1 mg HC/g rock	S_2 mg HC/g rock	S_1+S_2 mg HC/g rock	T_{max} °C	HI mg HC/g TOC	$EqVR_o$ %
XML–1	Shale	8.48	0.96	34.25	35.21	434	404	0.42
XML–2	Shale	2.19	0.50	7.03	7.53	432	321	/
XML–3	Shale	4.30	0.71	15.85	16.56	434	368	0.39
XML–4	Shale	14.10	1.66	62.73	64.39	442	445	0.39
XML–5	Shale	5.80	0.45	18.96	19.41	441	327	0.44
XML–6	Shale	4.56	0.72	21.5	22.22	439	472	0.46
XML–7	Shale	2.84	0.23	8.94	9.17	440	315	0.33

Abbreviations: S_1: free hydrocarbon; S_2: residual hydrocarbon; HI (Hydrogen Index) = S_2/TOC; the equivalent vitrinite reflectance ($EqVR_o$) values were calculated from vitrinite-like reflectance (R_v) based on the formula reported by Luo et al. (2021): $EqVR_o = 1.07 \times R_v - 0.18$; "/": no data.

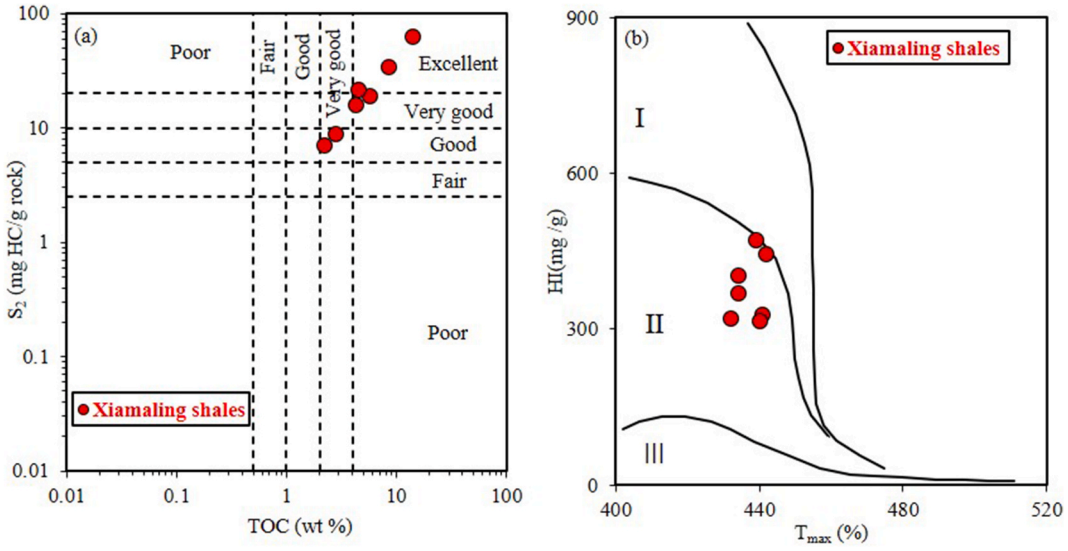

Fig. 3. (a) Plot of S_2–TOC; (b) plot of HI–T_{max}.

4. Results

4.1. Organic geochemical and petrological characteristics

The TOC contents of the Xiamaling shales vary from 2.19 to 14.10 wt %, averaging 6.04 wt % (Table 1 and Fig. 3a). The contents of S_1 and S_2 vary from 0.23 to 1.66 mg HC/g rock (av. = 0.75 mg HC/g rock) and 7.03–62.73 mg HC/g rock (av. = 24.18 mg HC/g rock), respectively (Table 1). The HI contents of the Xiamaling shales range from 315 to 472 mg HC/g TOC (av. = 378.87 mg HC/g TOC). The maximum pyrolysis peak temperature (T_{max}) of the samples ranges from 432 to 442 °C, with a mean of 437 °C (Table 1). OM type of the Xiamaling shales can be classified as type II (Fig. 3b).

The OM components in the Xiamaling shales are mainly algal-derived liptinite macerals, including lamalginite, bituminite, matrix bituminite, and vitrinite-like maceral (Fig. 4), which is similar to the maceral composition of the Hongshuizhuang, Barney Creek and Velkerri Formation (Crick et al., 1988; Crick, 1992; Luo et al., 2014). Bituminite with yellowish brown fluorescence is the most abundant component, and the lamalginite with yellowish or brown fluorescence is the second most abundant component (Fig. 4). Vitrinite-like maceral, as a primitive and autochthonous maceral, is widely distributed in the Xiamaling shales, and its occurrence is generally similar to vitrinite (Fig. 4). Thus, its reflectance is usually applied to evaluate the thermal maturity (Khan et al., 2020; Luo et al., 2021 Xiao et al., 2000). The equivalent vitrinite reflectance ($EqVR_o$) calculated from the vitrinite-like maceral reflectance in the Xiamaling shales are low (range: 0.33%–0.46%, averaging 0.41%, Table 1) (Luo et al., 2021), demonstrating that the studied shales are immature.

4.2. Elemental composition

The element composition details of the Xiamaling shale, including major and minor elements, REEs and their ratios are shown in Tables 2–4.

The sedimentary environment of the Xiamaling shales is determined according to the contents of Na, Ce and B and the comparison with the lacustrine Big Marsh oil shales of Nova Scotia (Fig. 5). The CIA, ICV, and PIA values in the Xiamaling shales, as parameters to get holistic information about chemical weathering, are in the range of 69.58–78.81 (av. = 73.65), 0.76–1.06 (av. = 0.88), 85.31–97.00 (av. = 91.49), respectively.

Some redox-susceptive trace elements, such as Mo, U, V, Ni, Co, Th and their ratios supply evidence about the depositional location in redox boundary during sedimentation and change of redox conditions with depth (Table 3). The V/(V + Ni), Ni/Co and Th/U values of these studied shales are in the range of 0.46–0.70 (av. = 0.60), 4.72–33.04 (av. = 18.50) and 1.80–4.16 (av. = 2.79), respectively (Table 3). The enrichment factors of Mo_{EF} and U_{EF} range from 2.50 to 13.28 and from 4.09 to 8.23 (Table 3). The variation in Mg vs Ca and Mn/Ca vs Sr/Ca values were applied to calculate the contents of terricolous influx and relative water temperature.

The contents of the REEs, the heavy rare earth elements (HREE), the light rare earth elements (LREE) in each sample, and their relations with other elements are presented as shown in Table 4. The average contents of ΣREE, HREE and LREE are 124.94, 40.52 and 84.42 ppm, respectively (Table 4). The provenance is determined based on the plots of Co/Th vs La/Sc and La/Th vs Hf, presented as follows (Table 4). The Co/Th and La/Sc values in the Xiamaling shales are relatively low and stable (0.22–0.75 and 2.55–3.44), with a mean of 0.43 and 3.02, respectively

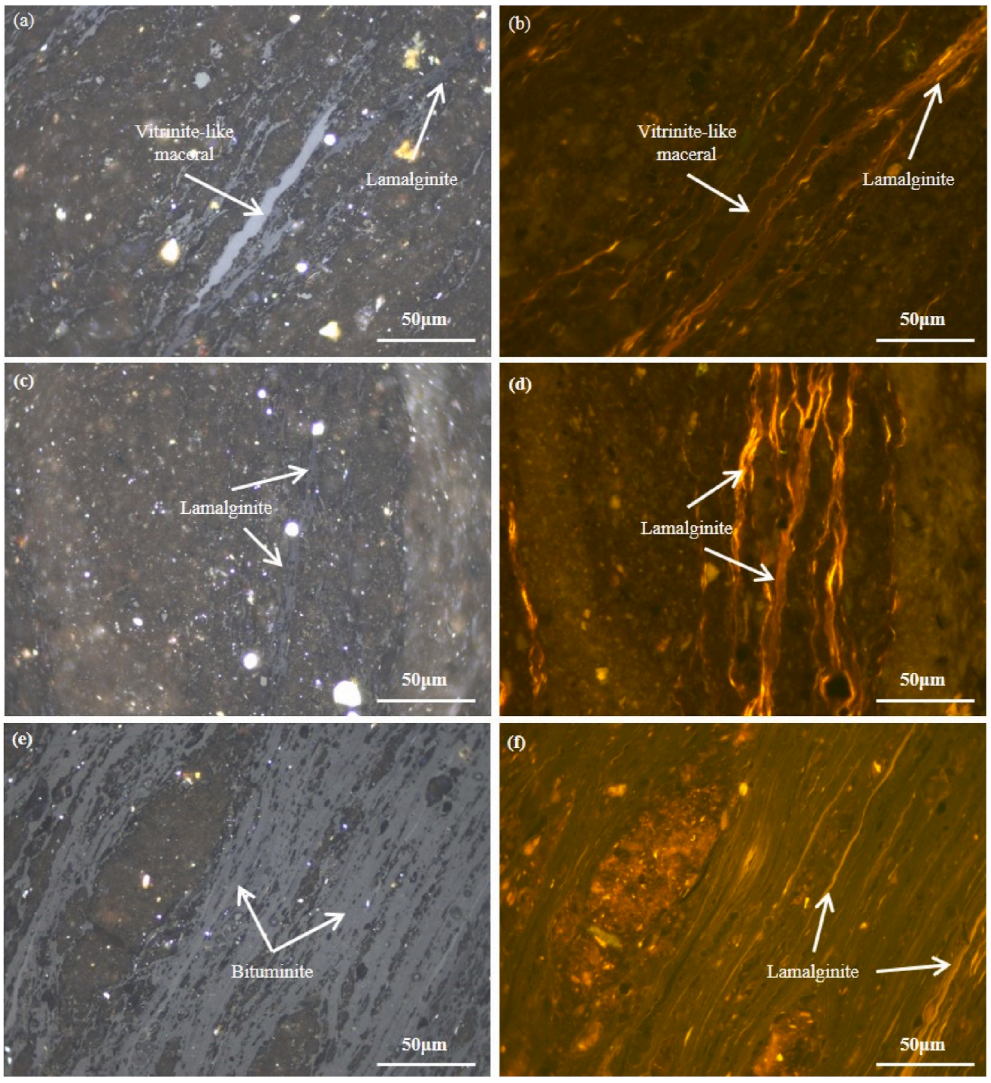

Fig. 4. Typical macerals of the Xiamaling shales. (a) Vitrinite-like maceral and lamalginite, reflected light, XML–6; (b) the identical field of view (a), fluorescence light; (c) Lamalginite, reflected light, XML–6; (d) the same field of view (c), fluorescence light; (e) Bituminite, reflected light, XML–6; (f) the same field of view (e), fluorescence light.

Table 2
Contents of major elements (ppm) for the marine Xiamaling shales.

Sample	XML–1	XML–2	XML–7	XML–3	XML–4	XML–6	XML–5
Zone	Coastal	Coastal	Coastal	Marginal	Marginal	Marginal	Open
Si	334,260	388,894	387,074	371,681	312,526	372,690	327,455
Al	38,217	36,365	32,577	39,485	38,583	36,326	55,327
Ca	3554	3376	3292	3677	4396	4342	4402
Fe	24,274	10,744	14,938	10,037	12,583	11,819	18,326
K	13,362	15,515	11,918	18,162	17,883	16,642	24,842
Mg	10,368	7021	8543	7076	7362	7612	10,734
Na	444	338	1043	760	1924	1716	1630
Ti	1794	1565	1323	1432	1913	1432	2468
CIA	78.81	75.96	75.31	73.37	69.58	70.06	72.50
PIA	96.53	97.00	90.86	93.79	85.31	86.04	90.89
ICV	1.06	0.78	0.95	0.76	0.88	0.88	0.83

(Table 4). The values of La/Th and Hf in the Xiamaling shales vary from 2.30 to 3.23 (av. = 2.80) and from 2.19 to 3.37 ppm (av. = 2.72 ppm), respectively (Table 4). The detailed data of the lacustrine Big Marsh oil shale can be found in Goodarzi et al. (2019a).

5. Discussion

5.1. Depositional environment

The marine Xiamaling shale was compared with the lacustrine Big Marsh oil shales, Nova Scotia, Canada to infer their sedimentary

Table 3
Contents of minor elements (ppm) for marine Xiamaling shale.

Sample	XML–1	XML–2	XML–7	XML–3	XML–4	XML–6	XML–5
Zone	Coastal	Coastal	Coastal	Marginal	Marginal	Marginal	Open
B	61.36	56.46	56.25	73.64	79.21	76.61	111.08
Co	3.07	2.65	1.73	1.25	4.67	2.03	7.63
Cu	79.00	26.80	35.70	53.70	88.30	51.90	79.80
Zr	100.00	88.00	82.80	97.70	104.00	101.00	127.00
Mn	75.13	50.58	50.55	41.10	69.56	47.61	68.06
Mo	6.04	1.08	1.63	3.67	5.83	2.61	2.89
Ni	56.10	24.00	42.05	41.30	65.20	52.90	36.00
Rb	51.10	56.40	46.65	58.10	68.30	54.00	112.00
Sc	6.46	6.16	4.91	5.41	7.79	5.32	10.30
Sr	44.20	35.80	42.00	77.80	38.40	38.90	52.00
Th	7.70	6.14	5.22	5.74	8.59	6.11	10.20
U	2.49	1.93	2.91	2.81	2.69	3.01	2.45
V	55.50	35.20	75.95	97.50	56.60	108.00	55.40
Mo_{EF}	13.28	2.50	4.21	7.81	12.70	6.03	4.38
U_{EF}	6.01	4.90	8.23	6.57	6.44	7.65	4.09
Sr/Cu	0.56	1.34	1.18	1.45	0.43	0.75	0.65
Rb/Sr	1.16	1.58	1.11	0.75	1.78	1.39	2.15
Ni/Co	18.27	9.06	24.38	33.04	13.96	26.06	4.72
Th/U	3.09	3.18	1.80	2.04	3.19	2.03	4.16
V/(V + Ni)	0.50	0.59	0.64	0.70	0.46	0.67	0.61

Table 4
Contents of REEs (ppm) in marine Xiamaling shale.

Sample	XML–1	XML–2	XML–7	XML–3	XML–4	XML–6	XML–5
Zone	Coastal	Coastal	Coastal	Marginal	Marginal	Marginal	Open
La	17.70	17.30	16.85	17.20	23.30	18.20	26.30
Ce	31.00	31.00	32.90	27.80	44.80	30.50	49.20
Pr	4.49	4.46	4.40	4.26	7.01	4.94	6.02
Nd	17.00	17.10	17.25	15.70	29.10	19.00	22.20
Sm	3.52	3.53	3.33	3.28	6.80	4.10	4.29
Eu	0.61	0.64	0.62	0.61	1.20	0.75	0.72
Gd	3.27	3.29	3.08	3.06	6.84	4.15	3.92
Tb	0.55	0.53	0.52	0.52	1.08	0.66	0.63
Dy	3.54	3.39	3.34	3.42	6.23	4.22	3.80
Ho	0.75	0.71	0.74	0.75	1.20	0.92	0.77
Er	2.25	2.16	2.42	2.41	3.40	2.80	2.32
Tm	0.35	0.33	0.38	0.37	0.48	0.43	0.35
Yb	2.40	2.30	2.67	2.61	3.23	2.93	2.42
Lu	0.38	0.36	0.43	0.42	0.48	0.47	0.37
Y	21.60	22.30	23.15	23.70	35.00	27.90	22.20
Eu_{an}	0.54	0.57	0.59	0.58	0.53	0.55	0.53
∑REE	109.40	109.39	112.06	106.11	170.15	121.96	145.51
La/Sc	2.74	2.81	3.44	3.18	2.99	3.42	2.55
Co/Th	0.40	0.43	0.33	0.22	0.54	0.33	0.75
La/Th	2.30	2.82	3.23	3.00	2.71	2.98	2.58
LREE	74.32	74.03	75.34	68.85	112.21	77.49	108.73
HREE	35.08	35.37	36.72	37.26	57.94	44.47	36.77

environments. The lacustrine Big Marsh oil shale has lower boron content (28–49 ppm), typical of freshwater lacustrine (Goodarzi, 1987, 2018). The Xiamaling shales have higher and variable boron content (56–110 ppm) (Table 3), typical of brackish water depositional setting (Fig. 5a) (Goodarzi and Swaine, 1994). The depositional environment of these two shales was very different. The Xiamaling Formation was mainly deposited in deep and quiet water below the storm wave base (>100 m) (Zhang et al., 2015). The sediment charged to the Yanshan basin was mostly wind-blown or due to the rivers input (Goodarzi, 2020; Wang et al., 2018; Zhang et al., 2019).

The lacustrine oil shale had a higher rate of terrestrial sediment input than the marine shale, suggested by the contents of Na and Ce (Fig. 5b). The lacustrine oil shales generally contain lower B, and higher Ce and ∑REE, indicating the higher input of the terrestrial sediments into a freshwater lake (Fig. 5a). By comparison, the Xiamaling shales have lower terricolous influx supported by the higher and mutable B (boron; 56–110 ppm) and lower Ce content, in agreement with Zhang et al. (2018).

The Xiamaling shales were deposited in a closed basin, limited environments, similar to an ancient lake (Diamond et al., 2018). However, Zhang et al. (2019), based on the detailed geochemical research, disputed this view and proposed that the sedimentary environment of the Xiamaling shales were marine and open, and the source of the basin sediments was vicinal rivers and atmospheric deposition. The present results indicate a variation of water chemistry due to freshwater input by the river(s) into the basin, resulting in low B and slightly brackish in the coastal area (Fig. 6a). The water is becoming brackish from the shallow towards the open marine, and the concentration of both Rb and ∑REE increases from coastal to the open marine (Fig. 6), which is due to a decrease in the terrestrial influx from coastal to open marine and an increase in the input of aluminosilicates (clay minerals) in the deep marine facies (Fig. 6b). This indicates a depositional classification and progressive sedimentation of fine clay towards the deep facies (Goodarzi, 2020). In general, this apparent variation in shale geochemistry related to the freshwater input would have been perhaps less noticeable if their deposition environment was restricted.

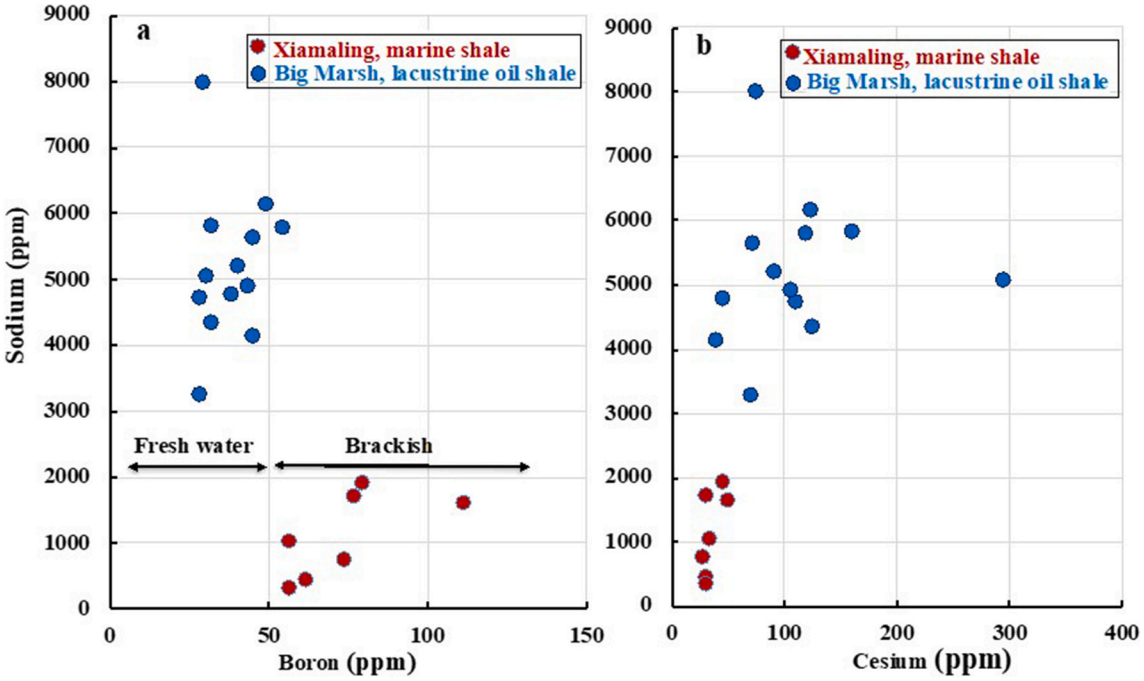

Fig. 5. Variation of sodium with (a) boron and (b) cesium for the lacustrine Big Marsh and marine Xiamaling shales (Goodarzi et al., 2019a, 2020).

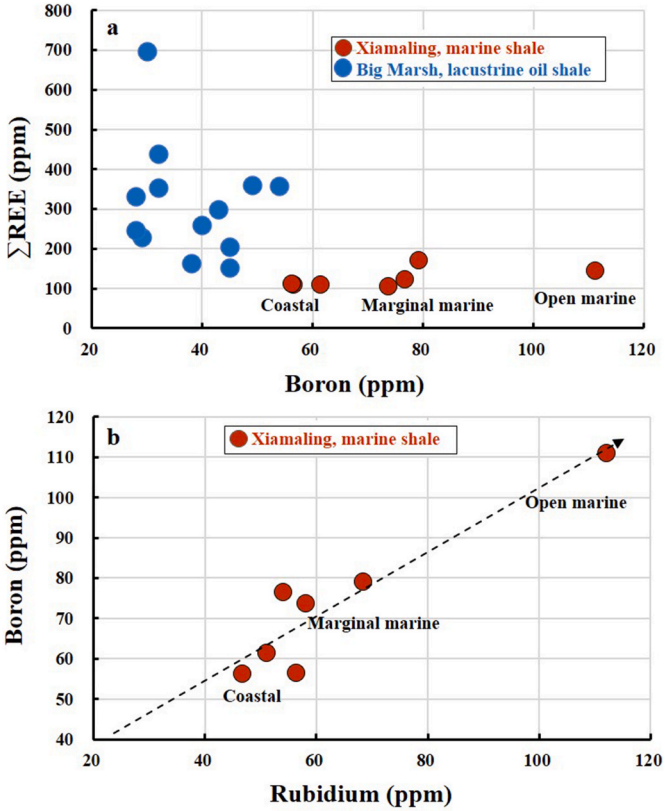

Fig. 6. The relation between boron with (a) total REEs for the Big Marsh lacustrine and Xiamaling marine shales (Goodarzi et al., 2019a, 2020), and (b) Rb for the Xiamaling marine shales.

Comparison of the Xiamaling shale with the Canadian marine and lacustrine oil shales was also conducted on the basis of the B and Ce variation (Bloch et al., 1999; Goodarzi et al., 2019a, 2020) (Fig. 7). The Xiamaling shale grouped with the marine Second White Speckled oil shale, Saskatchewan, Canada, followed a similar pattern related to the distance from the coast and depth (Fig. 7).

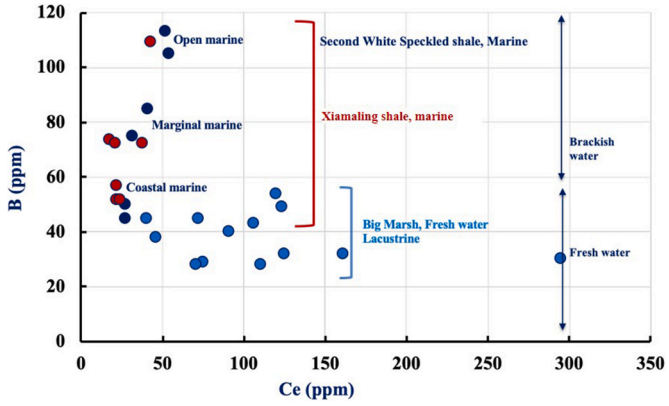

Fig. 7. The relation between the Xiamaling, the marine Second White Speckled and Big Marsh lacustrine oil shales based on the concentration of boron and cerium (Bloch et al., 1999; Goodarzi et al., 2019a, 2020).

5.2. *Provenance and chemical weathering*

The La/Sc and Co/Th ratios have sensitive responses to the provenance (Cullers, 1994; Luo et al., 2015b; Sun et al., 2008), since basic and siliceous rocks enrich La and Th, whereas Sc and Co are depleted (Cullers, 1994). The relatively low and stable values of Co/Th and La/Sc in the Xiamaling shales indicate a felsic source (Table 4 and Fig. 8a) (Gu et al., 2002; Luo et al., 2015b), which is consistent with the TiO_2–Zr diagram (Fig. 8b) (Hayashi et al., 1997).

The elemental composition of the island arc from the felsic source is characterized by the low and stable ratio of La/Th (<5) with the low contents of Hf ranging from 3 to 7 ppm (Floyd and Leveridge, 1987; Luo et al., 2015b; Xie et al., 2019). The low values of La/Th and Hf in the Xiamaling shales also indicate a felsic source, similar to the PAAS (Fig. 8c).

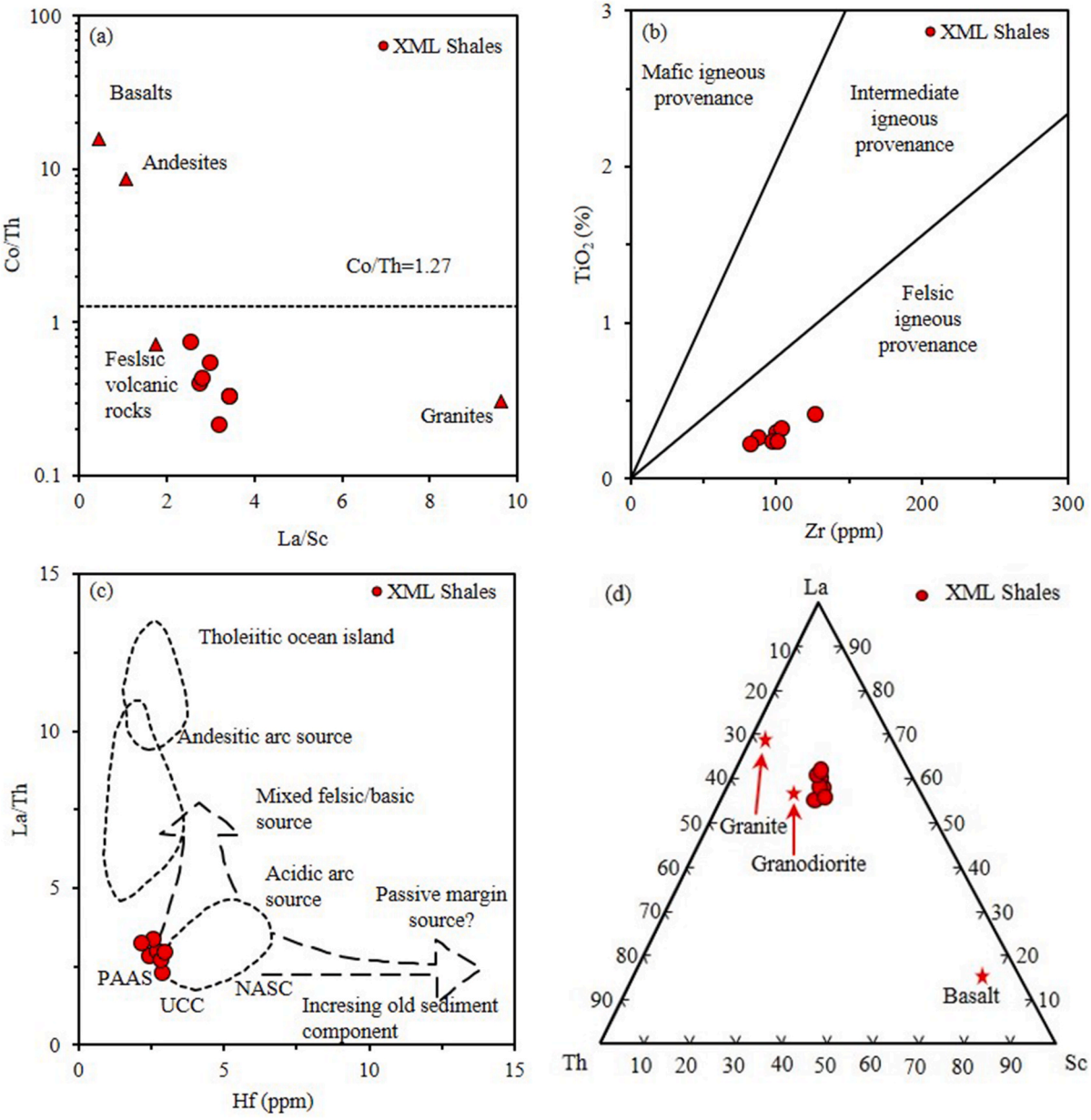

Fig. 8. Source identification diagrams of the Mesoproterozoic Xiamaling shales. (a) La/Sc–Co/Th (Gu et al., 2002); (b) TiO_2–Zr (Hayashi et al., 1997); (c) Hf–La/Th (Floyd and Leveridge, 1987); (d) Ternary La–Th–Sc plot. The location of granite, granodiorite and basalt in the figure is cited from Cullers and Podkovyrov (2000). Abbreviation: XML shales = Xiamaling shales.

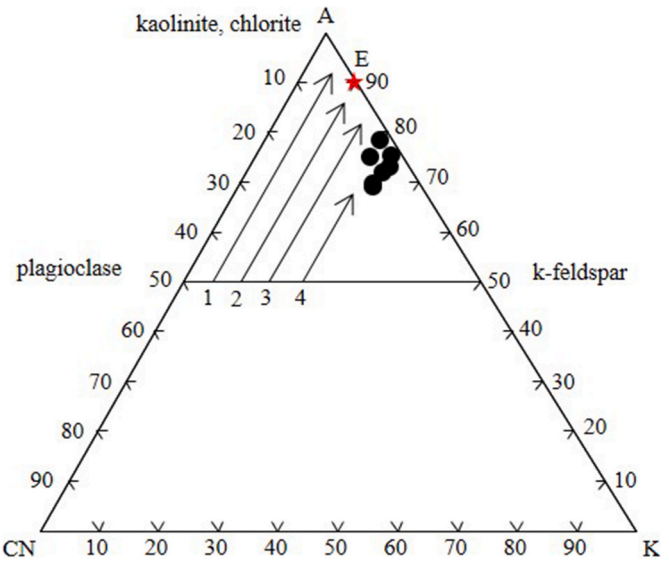

Fig. 9. Ternary diagram of A–CN–K for the Mesoproterozoic Xiamaling shales, North China (Nesbitt and Young, 1982). Numbers 1–4 represent different weathering trends in the different source rocks: 1–tonalite; 2–granodiorite; 3–adamellite; 4–granite. Point E is the intersection of line 2 and A–K boundary.

The provenance of sedimentary rocks can also be distinguished by the abundances of the REE (Fedo et al., 1996; Luo et al., 2015b). Generally, the negative Eu_{an} (Eu_{an} = 0.53–0.59, av. = 0.56) and high LREE/HREE ratios (LREE/HREE = 1.80–2.75, averaging 2.08, Table 4) imply felsic source rocks for the Xiamaling shales (Cullers and Graf, 1984; Taylor and McLennan, 1985), and their provenance is mainly granodiorite as indicated by the La–Th–Sc ternary diagram (Fig. 8d).

The stability of the elements is different during the chemical weathering of the rocks. Thus, the CIA and PIA can be applied to evaluate chemical weathering degree (Fedo et al., 1995; Nesbitt and Young, 1982). CIA = 50–60, 60–80 and 80–100 indicate low, moderate, and extreme chemical weathering intensity, respectively (Fedo et al., 1995; Selvaraj and Chen, 2006). The CIA values in the Xiamaling shales are 69.58–78.81 (av. = 73.65) (Table 2), demonstrating a moderate chemical weathering. The PIA values of the Xiamaling Formation shales are 85.31–97.00 (with the mean of 91.49) (Table 2), also indicating an intense chemical weathering in the source area (Fedo et al., 1995). The ICV of the Xiamaling shales are 0.76–1.06 (with an average of 0.88) (Table 2), mostly lower than 1, implying predominant proportion of the clay minerals in comparison to the rock forming minerals (Cox et al., 1995). The low ICV values also suggest strong chemical weathering of the source of the Xiamaling shales (Samad et al., 2020; Varma et al., 2018).

The chemical weathering intensity indicated by CIA values is slightly different from that indicated by PIA values, which may be due to the influence of potassium metasomatism. A–CN–K (A = Al_2O_3, CN= CaO* + Na_2O, K=K_2O) ternary has been used to characterize chemical weathering intensity and potassium metasomatism (Fedo et al., 1995; Nesbitt and Young, 1982; Luo et al., 2015b). With the increase of the chemical weathering, the evolution trend of chemical composition of the residues is firstly along the trend parallel to A–CN line, then parallel to A–K line towards apex A (Fig. 9). However, the Xiamaling shales have deviated from the weathering path of granodiorite (i.e., line 2 and line E–A) and move towards apex K (Fig. 9), indicating that K is relatively enriched and significant potassium metasomatism occurred, which results in low CIA values in the Xiamaling shales. This indicates that the corrected CIA values shall be higher than 90 (the value of point E in Fig. 9) and a strong chemical weathering occurred in the source area (Luo et al., 2015b).

5.3. Redox condition

Some susceptible trace elements, such as Co, Mo, Ni, V, and U, record the information of sedimentary redox boundary during deposition (Dean et al., 1997, 1999; Goodarzi et al., 2019a, 2020; Kremling, 1983; Jacobs et al., 1985; Tribovillard et al., 2006). Thus, their content and ratios (e.g., V/(V + Ni), Ni/Co and Th/U) can be used as the criteria for redox discrimination in the water column (Hatch and Leventhal, 1992; Hartkopf-Froder et al., 2007; Kimura and Watanabe, 2001; Liu et al., 2019, 2021).

The ratios of V/(V + Ni), Ni/Co and Th/U can also be used as indicators of the depositional conditions (Hartkopf-Froder et al., 2007; Hatch and Leventhal, 1992; Jones and Manning, 1994; Kimura and Watanabe, 2001; Li et al., 2021; Wignall and Twitchett, 1996). The Ni/Co, V/(V + Ni) and Th/U values show that the Xiamaling shales are generally deposited under dysoxic–anoxic environment (Table 3 and Fig. 10a, b and c). Luo et al. (2015a) also found that the Xiamaling shales from adjacent areas in the Xiahuayuan deposited under anoxic environments according to the V/(V + Ni) vs Th/U ratios (Fig. 10a).

Since Mo is relatively richer than U in partial anoxic environment, the redox environment of the sedimentary period can be studied by the relationship Mo–U in the redox environment (Algeo and Tribovillard, 2009; Zhu et al., 2022). In the Xiamaling shales, Mo enrichment is slightly higher than U. According to the Mo_{EF}–U_{EF} covariation model (Fig. 10d) (Algeo and Tribovillard, 2009), the Xiamaling shales were deposited under dysoxic–anoxic conditions, consistent with the redox-sensitive element ratios. Song et al. (2021) reported that the Xiamaling shales had a low pristane/phytane (Pr/Ph) ratio of <1.0 (with an average of 0.60), suggesting an anoxic condition (Didyk et al., 1978).

5.4. Paleotemperature

The Xiamaling shales were deposited in a tropical to sub-tropical environment with the latitude of 10°Ñ30°N (Zhang et al., 2012a), which were evident by the variation of Mg and Ca, when compared with the Big Marsh lacustrine oil shales, which were deposited in a temperate climate (Fig. 11) (Goodarzi, 2020). In general, the mineralogy of carbonate varies over time, as the stability of different carbonate minerals varies under different pressure and temperature conditions. The only stable phase of $CaCO_3$ is calcite at normal earth environment, and occurs as high-Mg calcite (11–20 mol% of $MgCO_3$) and low-Mg calcite (5 mol% of $MgCO_3$). The $MgCO_3$ content of the primordial calcite is dominated by temperature. The $MgCO_3$ is greater at higher temperatures (Mucci, 1987), as evidenced by the high Mg content in the Xiamaling shales deposited in a hot tropical climate (Wang et al., 2017), unlike the Big Marsh lacustrine oil shale, which was deposited under cooler temperate climate (Goodarzi, 2020). The high-Mg calcite is metastable at a lower temperature but converts to low-Mg calcite or dolomite overtime (Mackenzie et al., 1983). The variations of Mg–Ca for the lacustrine Big Marsh and marine Xiamaling shales reveal a higher temperature of the marine shales than the lacustrine Big Marsh oil shales (Fig. 11).

Other indicators of paleotemperature are Sr and Mn (Stoll et al., 2002). The lacustrine oil shales have higher terrigenous input and cooler temperature than the marine Xiamaling shales as indicated by the higher Mn content in the former oil shales. (Fig. 12a). The Sr/Ca vs Mn/Ca values were also applied to evaluate the paleotemperature and sedimentary influx (Fig. 12b). The high Mn/Ca value reveals a higher terrigenous influx, and high Sr/Ca is typically indicative of higher temperature (Stoll et al., 2002).

The lacustrine oil shales have low Sr/Ca and high Mn/Ca values (Fig. 12). The high Mn/Ca value is caused by high terricolous input, composed of large quantities of clay minerals and quartz (52.7 and 38 wt %) (Macauley and Bell, 1984). The low Sr/Ca value in the lacustrine oil shales with almost no carbonates indicates low temperature (Macauley and Bell, 1984). In contrast, the variety of Mn/Ca vs Sr/Ca for the Xiamaling shales demonstrated little sedimentary input, with warm

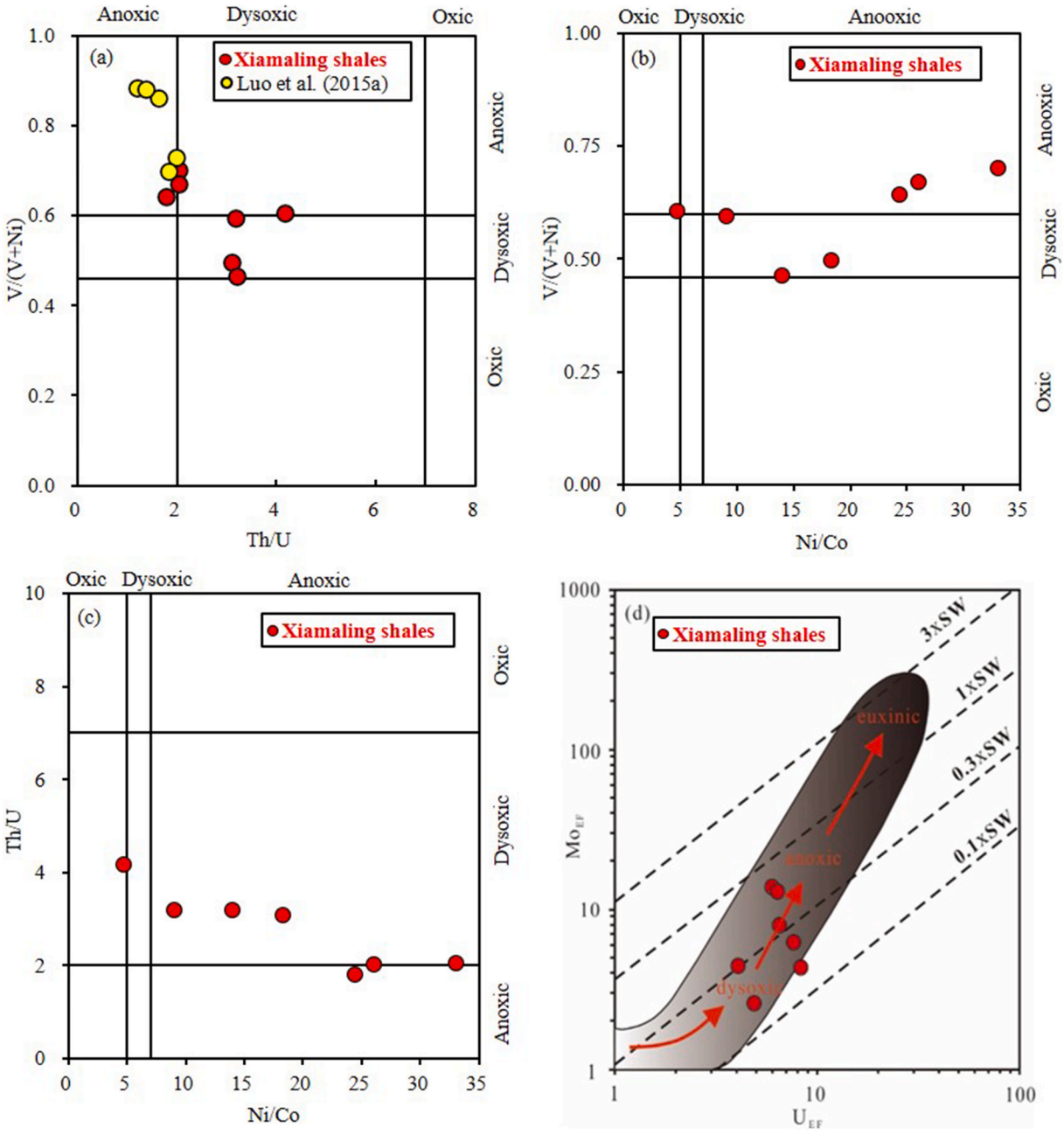

Fig. 10. Redox environment discrimination diagrams of Xiamaling Formation shales. (a) V/(V + Ni)–Th/U (Luo et al., 2015a); (b) V/(V + Ni)–Ni/Co; (c) Th/U–Ni/Co; (d) Mo_{EF}–U_{EF} covariant model (Algeo and Tribovillard, 2009). Abbreviation: SW = seawater molar ratio.

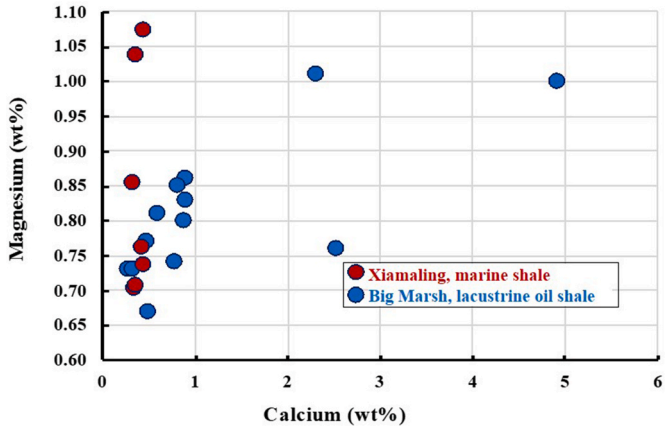

Fig. 11. Variation of Ca and Mg for marine Xiamaling and Lacustrine Big Marsh oil shales (Goodarzi et al., 2019a, 2020).

tropical water temperature (Fig. 12b).

5.5. Paleoclimate

The Sr/Cu ratio is a sensitive indicator of paleoclimate. Generally, Sr/Cu values > 10 suggest an arid climate, while values from 1 to 10 reflect a humid environment (Lerman, 1978). High Rb/Sr ratios reflect a relatively humid environment (Bai et al., 2015; Moradi et al., 2016). The Sr/Cu values in the Xiamaling shales are in the range of 0.44–1.45 (av. = 0.91), while the ratios of Rb/Sr range from 0.75 to 2.15 (av. = 1.34, Table 3 and Fig. 13), higher than the value in PASS (~0.80), indicating that the studied area was under relatively humid tropical climate, which was in agreement with the paleotemperature evidence as discussed earlier.

5.6. Rare earth elements

In the organic-rich sedimentary rock (coal, oil shales), the REEs are mainly connected with inorganic fractions related to the parent rock and weathering (Flier-Keller, 2009; Goodarzi et al., 2019a; Seredin and Dai, 2012). The REEs are generally concomitant with clay minerals and probably adsorbed on the surface of clay-size particles and minerals (Flier-Keller, 2009; Palmer and Filby, 1984). The variation in elemental concentration and REEs is also related to the depositional zones, and the concentration of Rb, B, and REEs increase from the coast towards the deep marine environment (Fig. 14).

Comparison of REEs, LREE, HREE and LREE/HREE ratio for the two shales reveals that the lacustrine oil shales have higher contents of ∑REEs and LREEs than the marine Xiamaling shales, due to higher terricolous input into the lacustrine environment than the marine one (Fig. 15). However, The HREEs in marine environment are greater than their equivalents in the costal lacustrine oil shale (Fig. 15).

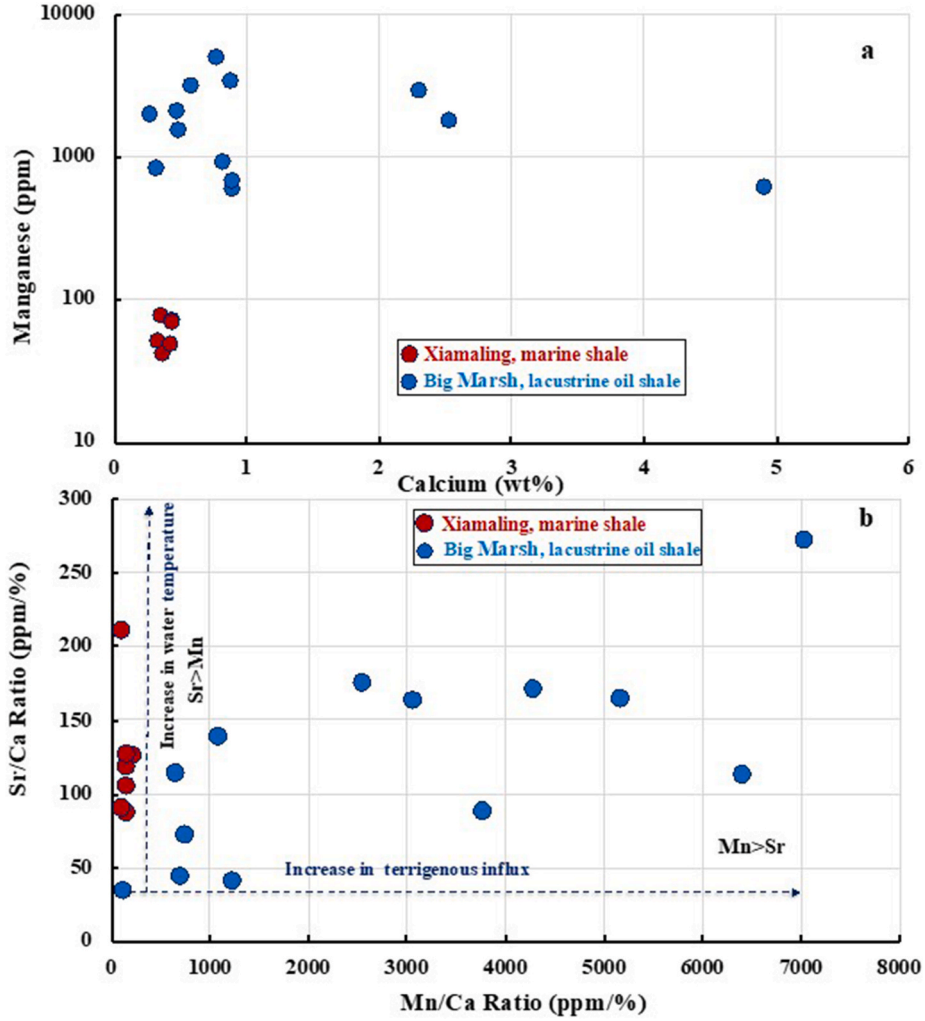

Fig. 12. Variation of (a) Calcium and Manganese, and (b) Mn/Ca vs Sr/Ca for marine Xiamaling and lacustrine Big Marsh oil shales (Goodarzi et al., 2019a, 2020).

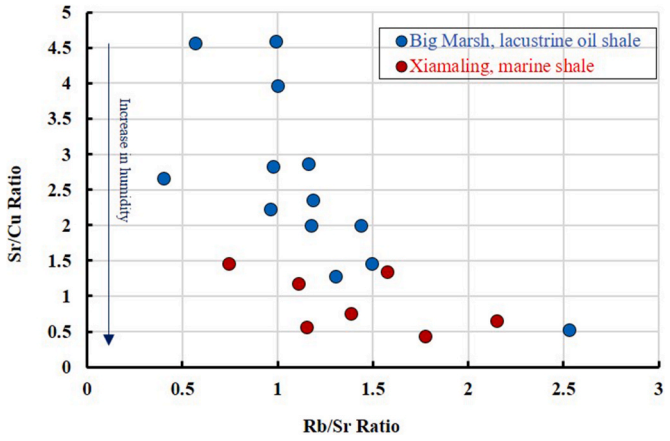

Fig. 13. Variation of Sr/Cu vs Rb/Sr ratios for marine Xiamaling and lacustrine Big Marsh oil shales (Goodarzi et al., 2019a, 2020).

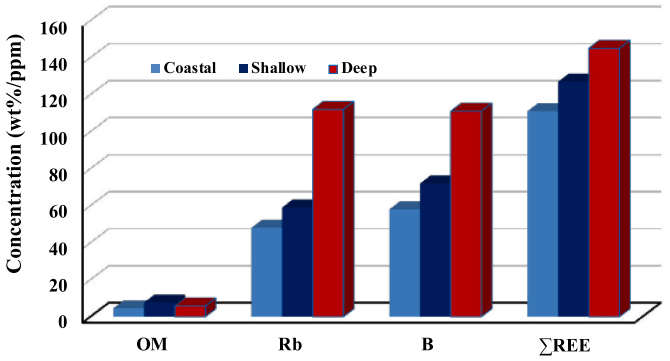

Fig. 14. Concentration of OM, Rb, B and total REEs for Xiamaling shales.

5.6.1. *Variation of PAAS-normalized REEs*

The REEs distribution modes in the Xiamaling shales were normalized to PAAS (Taylor and McLennan, 1985). These marine shales from three depositional zones follow similar patterns (Table 4 and Fig. 16a). There is a continuous increase from LREE towards HREE (Fig. 16a), typical of seawater (Alibo and Nozaki, 1999). All oil shales show weak negative Ce, typical of marine sediments (Alibo and Nozaki, 1999; Bau and Dulski, 1996). They also display moderate negative Eu anomalies, typical of the Post Archean Australian rock (Taylor and McLennan, 1985).

The potassium-rich rocks exhibit negative Eu anomaly, by comparison, the carbonate-rich sediment may show positive Eu anomaly, typical of seawater (Alibo and Nozaki, 1999; Leleyter and Probst, 1999). The PAAS-corrected REEs trends for both the Xiamaling and the marine Second White Speckled oil shales (Cretaceous age) display a negative Ce anomaly, typical sediments deposited under a marine environment (Fig. 16a and b). However, the Xiamaling shales show moderate negative Eu anomaly, similar to the lacustrine oil shale (Fig. 16c), typical of continental crust (Taylor and McLennan, 1985). The marine Second White Speckled oil shales show positive Eu (Fig. 16b), representative of carbonate-rich sediment (Bloch et al., 1999; Leleyter and Probst, 1999; Macrae et al., 1992). The moderate negative Eu anomaly of the Xiamaling shale is due to the presence of felsic volcanic rocks on the sea, providing an influx of the terrestrial quartz and clay particles into the sea, altering the REEs composition (Table 4 and Fig. 16a).

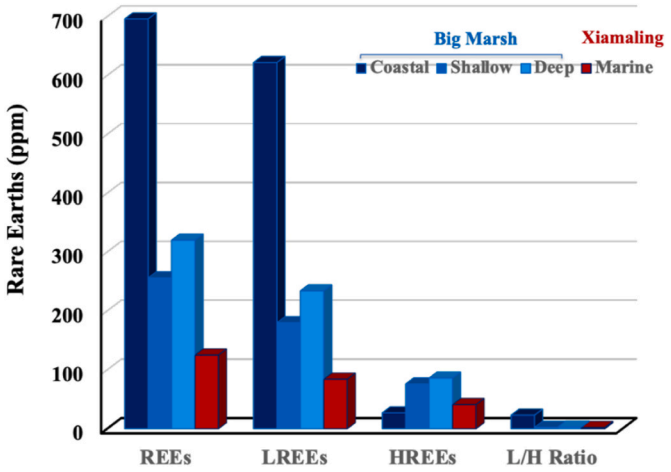

Fig. 15. Comparison of total REEs, LREE, HREE and ratio of L/H for the lacustrine Big Marsh oil shales and marine Xiamaling shales (Goodarzi et al., 2019a, 2020). Abbreviation: L/H = LREE/HREE.

5.7. *Hydrocarbon generation potential*

The hydrocarbon generation potential of the Xiamaling shale can be determined based on the maceral composition, TOC, rock pyrolysis parameters, and extractable OM (EOM) content. The Xiamaling shales have high TOC, S_1 and S_2 contents suggest that they are good to excellent hydrocarbon source rocks (Langford and Blanc-Valleron, 1990; Peters, 1986; Peters and Cassa, 1994) (Fig. 3a). Generally, the samples with HI $>$ 300 mg HC/g TOC are considered to have the capability of oil generation (Peters and Cassa, 1994). The HI values in the Xiamaling shales are in the range of 315–472 mg HC/g TOC, implying that they are oil-prone. This can be further proved by the abundant EOM in the Xiamaling shales (Song et al., 2021; Zhao et al., 2019). The Xiamaling shales show type II kerogen according to the HI–T_{max} diagram, suggesting their oil-prone property (Fig. 3b). These conclusions are consistent with abundant bituminite and lamalginite in the Xiamaling shales (Fig. 4).

6. Conclusions

The present results indicate that:

a. The Xiamaling shales were deposited under marine environments, including coastal, marginal, and open marine, with warm water temperature and humid tropical condition.
b. The elemental composition and ratios of the Xiamaling shales indicate the provenance of felsic volcanic rocks, which suffered moderate to strong chemical weathering.
c. The Xiamaling shales were deposited under dysoxic-anoxic condition.
d. The trend of PAAS normalized REEs in the Xiamaling shales displays negative Ce anomaly, typical of marine environment; and negative Eu anomaly, typical of continental setting, indicating little terrestrial influx.
e. The Xiamaling shales have good to excellent oil hydrocarbon generation potential with type II kerogen.

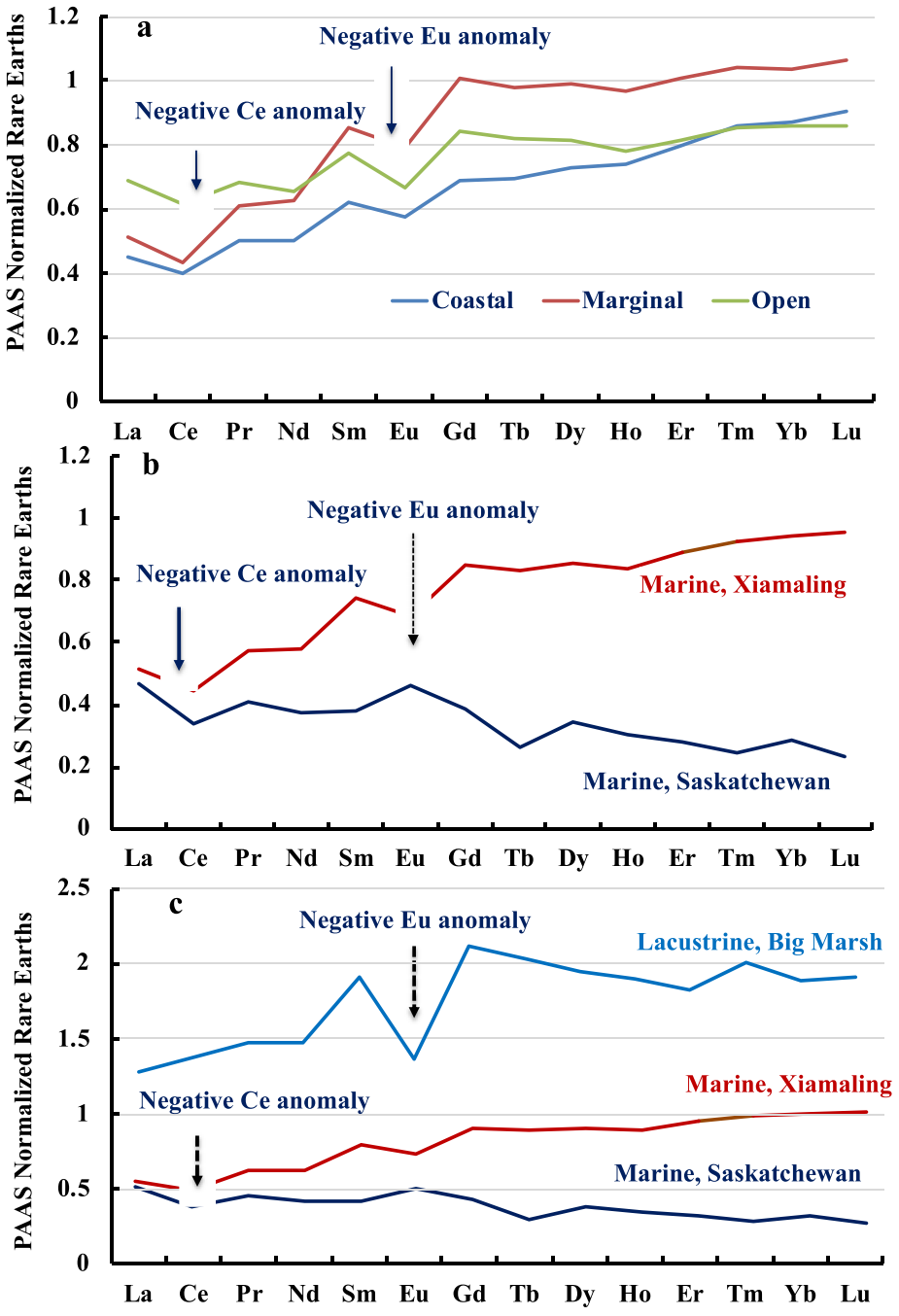

Fig. 16. Variation of PAAS normalized REEs trend for (a) average Xiamaling shales deposited in coastal, marginal, and deep environments, (b) average marine Xiamaling and Second White Speckled oil shales, and (c) average lacustrine and marine shales (Bloch et al., 1999; Goodarzi et al., 2019a, 2020).

Declaration of competing interest

The authors declare that they have no known competing financial interests or personal relationships that could have appeared to influence the work reported in this paper.

Acknowledgment

This work was supported by National Natural Science Foundation of China (No. 42122016 and 41773031), National Key Research and DevelopmentProgram of China (2017YFC0603102), and Science Foundation of China University of Petroleum, Beijing (2462020YXZZ021 and 2462021QNXZ001). Thanks to the State Key Laboratory of Petroleum Resources and Prospecting, China University of Petroleum (Beijing) for technical support and experimental analysis.

References

Algeo, T.J., Tribovillard, N., 2009. Environmental analysis of paleoceanographic systems based on molybdenum-uranium covariation. Chem. Geol. 268, 211–225.
Alibo, D.S., Nozaki, Y., 1999. Rare earth elements in seawater: particle association, shale-normalization, and Ce oxidation. Geochem. Cosmochim. Acta 63, 363–372.
Bai, Y., Liu, Z., Sun, P., Liu, R., Hu, X., Zhao, H., Xu, Y., 2015. Rare earth and major element geochemistry of Eocene fine-grained sediments in oil shale- and coal-bearing layers of the Meihe Basin, Northeast China. J. Asian Earth Sic. 97, 89–101.
Bau, M., Dulski, P., 1996. Distribution of yttrium and rare-earth elements in the Penge and Kuruman iron-formations, transvaal supergroup, South Africa. Precambrian Res. 79, 37–55.
Bloch, J.D., Schröder-Adams, C.J., Leckie, D.A., Craig, J., McIntyre, D.J., 1999. Sedimentology, micropaleontology, geochemistry and hydrocarbon potential of

shale from the Cretaceous lower Colorado group in western Canada. Geol. Surv. Can. Bull. 531, 185p.
Blumenberg, M., Thiel, V., Riegel, W., Kah, L.C., Reitner, J., 2012. Biomarkers of black shales formed by microbial mats, Late Mesoproterozoic (1.1 Ga) Taoudeni Basin, Mauritania. Precambrian Res. 196–197, 113–127.
Canfield, D.E., Zhang, S., Wang, H., Wang, X., Zhao, W., Su, J., Bjerrum, C.J., Haxen, E. R., Hammarlund, E.U., 2018. A Mesoproterozoic iron formation. Proc. Natl. Acad. Sci. U. S. A E3895–E3904.
Cox, R., Lowe, D.R., Cullers, R.L., 1995. The influence of sediment recycling and basement composition on evolution of mudrock chemistry in the southwestern United States. Geochem. Cosmochim. Acta 59 (14), 2919–2940.
Crick, I.H., 1992. Petrological and maturation characteristics of organic matter from the Middle Proterozoic McArthur Basin, Australia. Aust. J. Earth Sci. 39, 501–519.
Crick, I.H., Boreham, C.J., Cook, A.C., Powell, T.G., 1988. Petroleum geology and geochemistry of Middle Proterozoic McArthur Basin, northern Australia II: assessment of source rock potential 1. AAPG Bull. 72, 1495–1514.
Cullers, R.L., 1994. The controls on the major and trace element variation of shales, siltstones, and sandstones of Pennsylvanian-Permian age from uplifted continental blocks in Colorado to platform sediment in Kansas, USA. Geochem. Cosmochim. Acta 58, 4955–4972.
Cullers, R.L., Graf, J.L., 1984. Rare earth elements in igneous rocks of the continental crust: intermediate and silicic rocks-ore petrogenesis. Dev. Geochem. 2, 275–316.
Cullers, R.L., Podkovyrov, V.N., 2000. Geochemistry of the Mesoproterozoic Lakhanda shales in southeastern Yakutia, Russia: implications for mineralogical and provenance control, and recycling. Precambrian Res. 104, 77–93.
Dean, W.E., Gardner, J.V., Piper, D.Z., 1997. Inorganic geochemical indicators of glacial-interglacial changes in productivity and anoxia on the California continental margin. Geochem. Cosmochim. Acta 61, 4507–4518.
Dean, W.E., Piper, D.Z., Peterson, L.C., 1999. Molybdenum accumulation in Cariaco basin sediment over the past 24 k.y.: a record of water-column anoxia and climate. Geol. 27, 507–510.
Delpomdor, F., Blanpied, C., Virgone, A., Préat, A., 2013a. Paleoenvironments in meso–neoproterozoic carbonates of the mbuji-mayi supergroup (Democratic Republic of Congo) – microfacies analysis combined with C–O–Sr isotopes, major-trace elements and REE+Y distributions. J. Afr. Earth Sci. 88, 72–100.
Delpomdor, F., Linnemann, U., Boven, A., Rtner, A.G., Travin, A., Blanpied, C., Virgone, A., Jelsma, H., Préat, A., 2013b. Depositional age, provenance, and tectonic and paleoclimatic settings of the late Mesoproterozoic–middle Neoproterozoic Mbuji-Mayi Supergroup, Democratic Republic of Congo. Palaeogeogr. Palaeoclimatol. Palaeoecol. 389, 4–34.
Diamond, C.W., Planavsky, N.J., Wang, C., Lyons, T.W., 2018. What the ~1.4 Ga Xiamaling Formation can and cannot tell us about the mid-Proterozoic ocean. Geobiology 16, 219–236.
Fedo, C.M., Wayne Nesbitt, H., Young, G.M., 1995. Unraveling the effects of potassium metasomatism in sedimentary rocks and paleosols, with implications for paleoweathering conditions and provenance. Geol. 23, 921–924.
Didyk, B.M., Simoneit, B.R.T., Brassell, S.C., Eglinton, G., 1978. Organic geochemical indicators of paleoenvironmental conditions of sedimentation. Nature 272, 216–222.
Fedo, C.M., Eriksson, K.A., Krogstad, E.J., 1996. Geochemistry of shales from the Archean (~3.0 Ga) Buhwa Greenstone Belt, Zimbabwe: implications for provenance and source-area weathering. Geochem. Cosmochim. Acta 60, 1751–1763.
Flier-Keller, E.V.D., 2009. Rare earth elements in western Canadian coals. Energy Sources 15, 623–638.
Floyd, P.A., Leveridge, B.E., 1987. Tectonic environment of the Devonian Gramscatho basin, south Cornwall: framework mode and geochemical evidence from turbiditic sandstones. J. Geol. Soc. 144, 531–542.
Frank, T.D., Lyons, T.W., Lohmann, K.C., 1997. Isotopic evidence for the paleoenvironmental evolution of the mesoproterozoic Helena formation, Belt supergroup, Montana, USA. Geochem. Cosmochim. Acta 61, 5023–5041.
Goodarzi, F., 1987. Concentration of elements in lacustrine coals from zone A hat creek deposit No. 1, British Columbia, Canada. Int. J. Coal Geol. 8, 247–268.
Goodarzi, F., 2020. Comparison of the geochemistry of lacustrine oil shales of Mississippian age from Nova Scotia and new Brunswick, Canada. Int. J. Coal Geol. 220, 103398.
Goodarzi, F., Gentzis, T., 2018. Elemental concentration and organic petrology of unique liptinite-rich humic coal, canneloid shale, and cannel coal of Devonian age from Arctic Canada. Chem. Geol. 485, 44–55.
Goodarzi, F., Swaine, D.J., 1994. The influence of geological factors on the concentration of boron in Australian and Canadian coals. Chem. Geol. 118, 301–318.
Goodarzi, F., Gentzis, T., Sanei, H., Pedersen, P.K., 2019a. Elemental composition and organic petrology of a lower Carboniferous-age freshwater oil shale in Nova Scotia, Canada. ACS Omega 4, 20773–20786.
Goodarzi, F., Haeri-Ardakani, O., Gentzis, T., Pedersen, P.K., 2019b. Organic petrology and geochemistry of tournaisian-age Albert formation oil shales, new Brunswick, Canada. Int. J. Coal Geol. 205, 43–57.
Goodarzi, F., Nina, N.G., Malachowaka, A., 2021. Elemental composition, environment of deposition of the lower Carboniferous Emma Fiord formation oil shale in Arctic Canada. Int. J. Coal Geol. 103715.
Gu, X.X., Liu, J.M., Zheng, M.H., Tang, J.X., Qi, L., 2002. Provenance and tectonic setting of the proterozoic turbidites in Hunan, south China: geochemical evidence. J. Sediment. Res. 72, 393–407.
Hartkopf-Froder, C., Kloppisch, M., Mann, U., Neumann-Mahlkau, P., Schaefer, R.G., Wilkes, H., 2007. The end-Frasnian mass extinction in the Eifel Mountains, Germany: new insights from organic matter composition and preservation. Geol. Soc. Lond. Spe. Pub. 278, 173–196.
Hatch, J.R., Leventhal, J.S., 1992. Relationship between inferred redox potential of the depositional environment and geochemistry of the upper Pennsylvanian (Missourian) Stark shale member of the Dennis Limestone, Wabaunsee county, Kansas. U.S.A. Chem. Geol. 99, 65–82.
Hayashi, K.-I., Fujisawa, H., Holland, H.D., Ohmoto, H., 1997. Geochemistry of ~1.9 Ga sedimentary rocks from northeastern Labrador, Canada. Geochim. Cosmochim. Acta. 61, 4115–4137.
Jacobs, L., Emerson, S., Skei, J., 1985. Partitioning and transport of metals across the O_2H_2S interface in a permanently anoxic basin: Framvaren Fjord, Norway. Geochem. Cosmochim. Acta 49, 1433–1444.
Jones, B., Manning, D.A.C., 1994. Comparison of geochemical indices used for the interpretation of palaeoredox conditions in ancient mudstones. Chem. Geol. 111, 111–129.
Khan, I., Zhong, N., Luo, Q., Ai, J., Yao, L., Luo, P., 2020. Maceral composition and origin of organic matter input in neoproterozoic–lower Cambrian organic-rich shales of salt range formation, upper Indus basin, Pakistan. Int. J. Coal Geol. 217, 103319.
Kimura, H., Watanabe, Y., 2001. Oceanic anoxia at the Precambrian-Cambrian boundary. Geol. 29, 995–998.
Kremling, K., 1983. The behavior of Zn, Cd, Cu, Ni, Co, Fe, and Mn in anoxic baltic waters. Mar. Chem. 13, 87–108.
Langford, F.F., Blanc-Valleron, M.M., 1990. Interpreting Rock–Eval pyrolysis data using graphs of pyrolizable hydrocarbon vs. total organic carbon. AAPG Bull. 74, 799–804.
Leleyter, L., Probst, J.L., 1999. A new sequential extraction procedure for the speciation of particulate trace elements in river sediments. Int. J. Environ. Anal. Chem. 73, 109–128.
Lerman, A., 1978. Lakes–chemistry, geology, physics. J. Geol. 88, 249–250.
Li, T., Huang, Z, Chen, X., Li, X., Liu, J., 2021. Paleoenvironment and organic matter enrichment of the Carboniferous volcanic-related source rocks in the Malang Sag, Santanghu Basin, NW China. Petro. Sci. 18, 29–53.
Luo, Q., Zhong, N., Zhu, L., Wang, Y., Qin, J., Qi, L., Zhang, Y., Ma, Y., 2013. Correlation of burial organic carbon and paleoproductivity in the Mesoproterozoic Hongshuizhuang Formation, northern North China. Sci. Bull. 58, 1299–1309.
Luo, Q., Zhang, L., Zhong, N., Wu, J., Goodarzi, F, Sanei, H., Skovsted, C.B., Suchý, V., Li, M., Ye, X., Cao, W., Liu, A., Min, X., Pan, Y., Yao, L., Wu, J., 2021. Thermal evolution behavior of the organic matter and a ray of light on the origin of vitrinite-like maceral in the Mesoproterozoic and Lower Cambrian black shales: Insights from artificial maturation. Int. J. Coal Geol. 244, 103813.
Luo, Q., Zhong, N., Qin, J., Li, K., Zhang, Y., Wang, Y., Ma, L., 2014. Thucholite in Mesoproterozoic shales from northern north China: occurrence and indication for thermal maturity. Int. J. Coal Geol. 125, 1–9.
Luo, G., Hallmann, C., Xie, S., Ruan, X., Summons, R.E., 2015a. Comparative microbial diversity and redox environments of black shale and stromatolite facies in the Mesoproterozoic Xiamaling Formation. Geochem. Cosmochim. Acta 151, 150–167.
Luo, Q., Zhong, N., Wang, Y., Ma, L., Li, M., 2015b. Provenance and paleoweathering reconstruction of the mesoproterozoic Hongshuizhuang formation (1.4 Ga), northern North China. Int. J. Earth Sci. 104, 1701–1720.
Liu, Q., Li, P., Jin, Z., Liang, X., Zhu, D., Wu, X., Meng, Q., Liu, J., Fu, Q., Zhao, J., 2021. Preservation of organic matter in shale linked to bacterial sulfate reduction (BSR) and volcanic activity under marine and lacustrine depositional environments. Mari. Petr. Geol. 127, 104950.
Liu, Q., Zhu, D., Jin, Z., Meng, Q., Li, S., 2019. Influence of volcanic activities on redox chemistry changes linked to the enhancement of the ancient Sinian source rocks in the Yangtze craton. Precambrian Res. 327, 1–13.
Luo, Q., George, S.C., Xu, Y., Zhong, N., 2016. Organic geochemical characteristics of the Mesoproterozoic Hongshuizhuang Formation from northern China: implications for thermal maturity and biological sources. Org. Geochem. 99, 23–37.
Ma, K., Hu, S., Wang, T., Zhang, B., Qin, S., Shi, S., Wang, K., Huang, Q., 2017. Sedimentary environments and mechanisms of organic matter enrichment in the Mesoproterozoic Hongshuizhuang Formation of northern China. Palaeogeogr. Palaeoclimatol. Palaeoecol. 475, 176–187.
Macauley, G., Bell, F.D., 1984. Oil shales of the Big Marsh and Pictou areas, Nova Scotia. Geol. Surv. Canada. Open File Rep. 57, 1037.
Mackenzie, F.T., Bischoff, W.D., Bishop, F.C., Loijens, M., Schoomaker, J., Wollast, R., 1983. Magnesian calcites: low-temperature occurrence, solubility and solid-solution behavior. Rev. Mineral. Geochem. 11, 97–144.
Macrae, N.D., Nesbitt, H.W., Kronberg, B.I., 1992. Development of a positive Eu anomaly during diagenesis. Earth Planet Sci. Lett. 109, 585–591.
McLennan, S.M., Hemming, S., McDaniel K,, D, Hanson, G.N., 1993. Geochemical approaches to sedimentation, provenance, and tectonics. Spec. Papers-Geol. Soc. Am. 284, 21–40.
Meng, Q.R., Wei, H.H., Qu, Y.Q., Ma, S.X., 2011. Stratigraphic and sedimentary records of the rift to drift evolution of the northern North China craton at the Paleo- to Mesoproterozoic transition. Gondwana Res. 20, 205–218.
Mitchell, R.L., Sheldon, N.D., 2010. The ~1100 Ma Sturgeon Falls paleosol revisited: implications for Mesoproterozoic weathering environments and atmospheric CO_2 levels. Precambrian Res. 183, 738–748.
Moradi, A.V., Sari, A., Akkaya, P., 2016. Geochemistry of the Miocene oil shale (Hanili Formation) in the ankr-orum Basin, Central Turkey: implications for Paleoclimate conditions, source–area weathering, provenance and tectonic setting. Sediment. Geol. 341, 289–303.
Mucci, A., 1987. Influence of temperature on the composition of magnesian calcite overgrowths precipitated from seawater. Geochem. Cosmochim. Acta 51, 1977–1984.
Nesbitt, H.W., Young, G.M., 1982. Early Proterozoic climates and plate motions inferred from major element chemistry of lutites. Nature 299, 715–717.

Palmer, C.A., Filby, R.H., 1984. Distribution of trace elements in coal from the Powhatan No. 6 mine, Ohio. Fuel 63, 318–328.
Peters, K.E., 1986. Guidelines for evaluating petroleum source rock using programmed pyrolysis. AAPG Bull. 70, 318–329.
Peters, K.E., Cassa, M.R., 1994. Applied source rock geochemistry. In: Magoon, L.B., Dow, W.G. (Eds.), The Petroleum System-From Source to Trap, vol. 60. Amer. Asso. Petr. Geol., Memoir, pp. 93–120.
Qi, L., Hu, J., Gregoire, D.C., 2000. Determination of trace elements in granites by inductively coupled plasma mass spectrometry. Talanta 51, 507–513.
Rashid, S.A., Ahmad, S., Singh, S.K., Absar, N., 2018. Elemental and Sr-Nd isotopic geochemistry of Mesoproterozoic sedimentary successions from NE Lesser Himalaya, northern India: implications for Proterozoic climate and tectonics. J. Asian Earth. Sic. 163, 235–248.
Samad, S.K., Mishra, D.K., Mathews, R.P., Ghosh, S., Mendhe, V.A., Varma, A.K., 2020. Geochemical attributes for source rock and palaeoclimatic reconstruction of the Auranga Basin, India. J. Petrol. Sci. Eng. V. 185, 10665.
Selvaraj, K., Chen, C.-T.A., 2006. Moderate chemical weathering of subtropical Taiwan: constraints from solid-phase geochemistry of sediments and sedimentary rocks. J. Geol. 114, 101–116.
Seredin, V.V., Dai, S., 2012. Coal deposits as potential alternative sources for lanthanides and yttrium. Int. J. Coal Geol. 94, 67–93.
Song, D., Chen, Y., Wang, T., Li, M., Li, P., 2021. Organic geochemical compositions of mesoproterozoic source rocks in the Yanliao rift, northern China. Mar. Petrol. Geol. 123, 104740.
Stoll, H.M., Rosenthal, Y., Falkowski, P., 2002. Climate proxies from Sr/Ca of coccolith calcite: calibrations from continuous culture of Emiliania huxleyi. Geochem. Cosmochim. Acta 66, 927–936.
Sun, W.H., Zhou, M.F., Yan, D.P., Li, J.W., Ma, Y.X., 2008. Provenance and tectonic setting of the neoproterozoic Yanbian group, western Yangtze Block (SW China). Precambrian Res. 167, 213–236.
Taylor, S.R., McLennan, S.M., 1985. The continental crust: its composition and evolution. Geol. 94, 57–72.
Tribovillard, N., Algeo, T.J., Lyons, T., Riboulleau, A., 2006. Trace metals as paleoredox and paleoproductivity proxies: an update. Chem. Geol. 232, 12–32.
Varma, A.K., Mishra, D.K., Samad, S.K., Prasad, A.K., Panigrahi, D.C., Mendhe, V.A., Singh, B.D., 2018. Geochemical and organo-petrographic characterization for hydrocarbon generation from Barakar Formation in Auranga basin, India. Int. J. Coal Geol. 186, 97–114.
Wang, H., Qiao, X., 1984. Proterozoic stratigraphy and tectonic framework of China. Geol. Mag. 121, 599–614.
Wang, X., Zhang, S., Wang, H., Bjerrum, C.J., Hammarlund, E.U., Haxen, E.R., Su, J., Wang, Y., Canfield, D.E., 2017. Oxygen, climate and the chemical evolution of a 1400 million year old tropical marine setting. Am. J. Sci. 317, 861–900.
Wang, X., Zhao, W., Zhang, S., Wang, H., Su, J., Canfield, D.E., Hammarlund, E.U., 2018. The aerobic diagenesis of Mesoproterozoic organic matter. Sci. Rep. 8, 13324.
Wignall, P.B., Twitchett, R.J., 1996. Oceanic anoxia and the end Permian mass extinction. Science 272, 1155–1158.
Xiao, X., Wilkins, R.W.T., Liu, D., Liu, Z., Fu, J., 2000. Investigation of thermal maturity of lower Palaeozoic hydrocarbon source rocks by means of vitrinite-like maceral reflectance - a Tarim Basin case study. Org. Geochem. 31, 1041–1052.
Zhang, S.H., Zhao, Y., Yang, Z.Y., He, Z.F., Wu, H., 2009. The 1.35 Ga diabase sills from the northern North China Craton: implications for breakup of the Columbia (Nuna) supercontinent. Earth Planet Sci. Lett. 288, 588–600.
Xie, Q., Cai, Y., Dong, Y., Zhai, M., Li, D., 2019. Geochemical characteristics of the Permian marine mudstone and constraints on its provenance and paleoenvironment in the Fenghai area, Fujian Province, southeastern China. Petro. Sci. 16, 527–540.
Zhang, S., Li, Z.X., Evans, D.A.D., Wu, H., Li, H., Dong, J., 2012a. Pre-Rodinia supercontinent Nuna shaping up: a global synthesis with new paleomagnetic results from North China. Earth Planet Sci. Lett. 353–354, 145–155.
Zhang, S.H., Zhao, Y., Santosh, M., 2012b. Mid-Mesoproterozoic bimodal magmatic rocks in the northern North China Craton: implications for magmatism related to breakup of the Columbia supercontinent. Precambrian Res. 222–223, 339–367.
Zhang, S., Wang, X., Hammarlund, E.U., Wang, H., Costa, M.M., Bjerrum, C.J., Connelly, J.N., Zhang, B., Bian, L., Canfield, D.E., 2015. Orbital forcing of climate 1.4 billion years ago. Proc. Natl. Acad. Sci. U. S. A 112, E1406–E1413.
Zhang, S., Wang, X., Wang, H., Bjerrum, C.J., Hammarlund, E.U., Costa, M.M., Connelly, J.N., Zhang, B., Su, J., Canfield, D.E., 2016a. Sufficient oxygen for animal respiration 1,400 million years ago. Proc. Natl. Acad. Sci. U. S. A 113, 1731–1736.
Zhang, S., Wang, X., Wang, H., Bjerrum, C.J., Hammarlund, E.U., Dahl, T.W., Canfield, D. E., 2016b. Reply to Planavsky et al.: strong evidence for high atmospheric oxygen levels 1,400 million years ago. Proc. Natl. Acad. Sci. U. S. A 113, E2552–E2553.
Zhang, S., Wang, X., Wang, H., Hammarlund, E.U., Su, J., Wang, Y., Canfield, D.E., 2017. The oxic degradation of sedimentary organic matter 1400Ma constrains atmospheric oxygen levels. Biogeo 14, 2133–2149.
Zhang, K., Zhu, X., Wood, R.A., Shi, Y., Gao, Z., Poulton, S.W., 2018. Oxygenation of the Mesoproterozoic ocean and the evolution of complex eukaryotes. Nat. Geosci. 11, 345–350.
Zhang, S., Wang, X., Wang, H., Bjerrum, C.J., Hammarlund, E.U., Haxen, E.R., Wen, H., Ye, Y., Canfield, D.E., 2019. Paleoenvironmental proxies and what the Xiamaling Formation tells us about the mid-Proterozoic ocean. Geobiology 17, 225–246.
Zhao, W., Wang, X., Hu, S., Zhang, S., Wang, H., Guan, S., Ye, Y., Ren, R., Wang, T., 2019. Hydrocarbon generation characteristics and exploration prospects of Proterozoic source rocks in China. Sci. China Earth Sci. 62, 909–934.
Zhu, G., Li, T., Zhang, Z., Zhao, K., Song, H., Wang, P., Yan, H., Song, H., 2022. Nitrogen isotope evidence for oxygenated upper ocean during the Cryogenian interglacial period. Chem. Geol. 604, 120929.